RSC Advances

PAPER

View Article Online
View Journal | View Issue

Cite this: *RSC Adv.*, 2023, **13**, 10847

First-principles study on novel Fe-based quaternary Heusler alloys, with robust half-metallic, thermoelectric and optical properties†

Roshme Prakash and G. Kalpana *

Received 11th February 2023
Accepted 27th March 2023

DOI: 10.1039/d3ra00942d

rsc.li/rsc-advances

This work aims are studying new and unique Fe-based quaternary Heusler alloys for data storage, energy conversion and optoelectronics applications. The structural, magnetic, mechanical, electrical, thermal, and optical properties of novel FeCrYZ (Y = Ti, Zr, & Hf and Z = Sn, and Sb) alloys have been theoretically explored making use of density functional theory (DFT). Except for FeCrHfSb, all the alloys are found to exhibit a stable ferromagnetic ground state during the energy minimization process, also half metallic ferromagnetism exhibiting 100% spin-polarization at the Fermi level obeying Slater–Pauling rule with total integer magnetic moments of $2.00\mu_B$ and $1.00\mu_B$ respectively. FeCrTiSn, FeCrTiSb and FeCrZrSb alloys have mechanical and dynamical stability under ambient conditions. Boltzmann transport theory was used to investigate the thermoelectric performance of the materials in the temperature range of 100–900 K. The estimated dimensionless figure of merit (*ZT*) for FeCrTiSb is 1.76, FeCrZrSb is 0.61, and FeCrHfSb is 0.86 at 900 K. Optical spectra reveal that absorption occurs across the visible and near UV ranges of the region. Results show that the narrow bandgap, spin polarization and high *ZT* value of FeCrTiSb make it a promising candidate for spintronic, thermoelectric and optoelectronic applications.

Introduction

Thermoelectricity (TE) is viewed as a promising energy conversion technology with the potential to be among the most environmentally friendly and sustainable remedies to the world's growing energy crisis. Thermoelectric materials have the potential to use waste heat to generate electricity, which could be a useful alternative source of energy. They are employed in a wide range of applications, including refrigeration, power generation, and temperature measurement. The application possibilities are limited because the performance of a TE material is determined by the generally conflicting necessity for a material's physical properties: electrical conductivity should be high while thermal conductivity should be low. The thermoelectric efficiency of a material is measured using a dimensionless quantity called the figure of merit, $ZT = \frac{S^2\sigma}{\kappa}T$. Where S, σ, κ, and T, are the Seebeck coefficient, electrical conductivity, electronic thermal conductivity, and temperature respectively. These parameters (S, σ, κ_e) are related to the electronic component of thermal transport.

Heusler alloys, which were first found in 1903, are commonly utilized in electronic spin devices, such as magnetoresistive random access memory (MRAM),[1] giant magnetoresistance (GMR)[2] and magnetic sensors.[3] Heusler alloys (HA) were gaining attraction due to their extensive functional properties in electronics, spintronics, magnetism and thermoelectrics among other fields. The half-metallic (HM) character of these materials makes them particularly well-suited for use in magneto-electronic devices. A metallic-type band structure can be found in any of the two spin states of HM materials and a semiconducting-type band structure can be found in the other spin state as can be found in many HA. Quaternary Heusler Alloys (QHA) have attracted a lot of attention as a result of their special physical characteristics, which include a higher Curie temperature, strong magnetism, and a large energy gap. However, there hasn't been much research done on Fe-based QHA.

Many Heusler alloys have recently been discovered to offer TE qualities comparable to traditional Bi_2Te_3 and PbTe-based TE materials.[4] Fe-based Heusler alloys have recently been identified with thermoelectric and spintronic applications. The computed total magnetic moment of FeRhCrZ (Z = Si and Ge) is $3.00\mu_B$ per formula unit confirms that the alloys are half-metallic ferromagnets and reported maximum *ZT* of 0.45 at high temperature.[5] p-Type FeTaSb and n-type FeMnTiSb show high *ZT* values of 0.72 and 0.46 at 1100 K respectively.[6] The total spin magnetic moment of FeCr-based QHA is found to be 1.00 to $4.00\mu_B$ per formula unit confirms that the alloys are half-metallic ferromagnets in nature.[7] In recent years, half metallic, thermoelectric and optical properties in Heusler alloys

Department of Physics, Anna University, Chennai 600025, India. E-mail: roshmeprakash92@gmail.com; g_kalpa@annauniv.edu

† Electronic supplementary information (ESI) available. See DOI: https://doi.org/10.1039/d3ra00942d

and perovskite have received a lot of attention from researcher,[8–11] $XTiCl_3$ (X = Rb, Cs),[12] FeCrMnSb,[13] FeNbScZ (Z = Al, Ga, Ge, Si),[14] FeCrRuZ (Z = Al, Ga, In & Si),[15] Fe_2TaZ (Z = Al, Ga & In),[16] Fe_2VAl,[17] Fe_2TiZ (Z = Ga, Ge, As, In, Sn & Sb),[18] Fe_2TiSi, Fe_2TiGe and Fe_2ZrSi,[19] Fe_2CrSb,[20] Fe_2TaZ (Z = Al, Ga, In),[21] FeZrTiZ (Z = Si, Sn, Pb),[22] FeCrRuSi,[23] CoZrCrZ (Z = Al, Ga, In),[24] Mn_2MgGe,[25] XRuCrZ (X = Co, Ni, Rh and Pd; Z = Si and Ge),[26] XCaB (X = Li, Na, K and Rb),[27] ZrTiRhZ (Z = Ge, Sn),[28] CoFeVSb,[29] YFeCrZ (Z = Al, Sb & Sn),[30] CoFeXSn (X = Ru, Zr, Hf & Ta),[31] CoFeRGa (R = Ti, V, Cr, Mn, Cu and Nb),[32] MNiSn[33] Mn_2ZrX (X = Ge, Si).[34] Alloys have been discovered to be half-metallic. Additionally, in recent years, experimental research have examined the spintronics and thermoelectric application of Heusler compounds.[35–41] In this case, A. El-Khouly, *et al.* synthesized $FeV_{0.24}Nb_{0.4}Hf_{0.16}Ti_{0.2}Sb$ Heusler alloys by employing arc melting followed by induction melting and investigated the thermoelectric properties of these alloys.[39] Their method led to, with low thermal conductivity and figure of merit value of 0.44 at 725 K for $FeV_{0.24}Nb_{0.4}Hf_{0.16}Ti_{0.2}Sb$, suitable for thermoelectric applications. Deepika Rani *et al.* conducted a comprehensive experimental and theoretical investigation of the structural, electronic, magnetic, and transport properties of the quaternary Heusler alloys CoRuMnGe and CoRuVZ (Z = Al, Ga) for spintronic applications.[36] The experimental magnetic moments of CoRuMnGe and CoRuVGa are in close agreement with the theoretical values this result predicted by the Slater–Pauling rule.

As a first step, we examine and evaluate the detailed ground-state parameters of FeCrYZ (Y = Ti, Zr & Hf, Z = Sn & Sb) alloys, with a focus on electronic structure, mechanical, dynamical stability, magnetic, thermoelectric and optical properties. The remaining portion of this article are set up as follows: Computational details, Results and discussion and Conclusion.

Computational details

The present calculations for FeCrYZ (Y = Ti, Zr & Hf, Z = Sn & Sb) alloys are performed using the full-potential linearized augmented plane wave (FP-LAPW) technique within the density functional theory as implemented in the Wien2k code. The exchange–correlation potential was considered within the generalized gradient approximation (GGA) of Perdew–Burke–Ernzerhof (PBE)[42,43] and modified Becke–Johnson (mBJ)[44] potential. Often, GGA undervalues the energy gap of semiconductors; therefore, the modified Becke–Johnson potential (mBJ) was employed to obtain a more accurate energy gap. The thermoelectric transport properties were determined utilizing the semi-classical Boltzmann transport equation using the BoltzTraP code. A plane wave cut-off of R_{MT}. $K_{max} = 8.0$ in the interstitial range, with a maximum value of $l_{max} = 10$ is used. $G_{max} = 12$ was used to treat the Fourier expanded charge density. In the irreducible wedge of the Brillouin zone 3000 *k*-points are used for integration. During SCF calculations, the energy and charge are set to converge be 0.0001 Ry and 0.0001*e*, respectively. To compute the transport coefficients, a large *k*-point mesh with 120 000 *k*-points were employed. To study the dynamic stability of these alloys and the phonon dispersion spectra Quantum Espresso code is used, which is based on pseudopotentials and operates within the PBE framework.

Results and discussion

Structural and mechanical properties

Quaternary Heusler alloys (QHA) are intermetallic alloys that belong to the space group $F\bar{4}3m$ (no. 216) and have the stoichiometric formula XX′YZ.[45] The Fe and Cr atoms are located at the Wyckoff sites 4a (3/4, 3/4, 3/4) and 4b (1/4, 1/4, 1/4), Ti/Zr/Hf and Sn/Sb are situated on 4c (1/2, 1/2, 1/2) and 4d (0, 0, 0) respectively. The atomic arrangements in QHA are depicted in Fig. 1a. To evaluate the ground state properties, structural phase stability, as well as magnetic state of FeCrYZ (Y = Ti, Zr & Hf, Z = Sn & Sb) alloys, total energy is examined in a basis of relative volume and fit onto a Birch–Murnaghan equation of state.[46,47] To illustrate, the total energy curve relates to the relative volume of FeCrTiSb in nonmagnetic (NM) and ferromagnetic states (FM) is depicted in Fig. 1b. Table 1 shows the equilibrium lattice constants and ΔE, which is the difference in energy between NM and FM ($\Delta E = E_{NM} - E_{FM}$). It is indicated

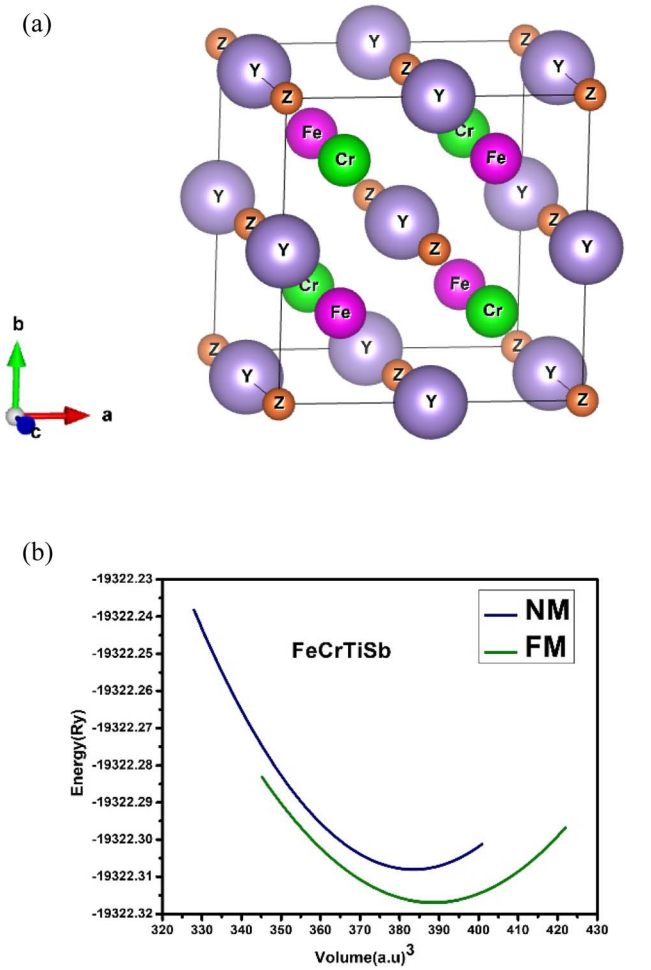

Fig. 1 (a) The crystal structure of FeCrYZ (Y = Ti, Zr, & Hf, Z = Sn & Sb) quaternary Heusler alloys. (b) Total energy *vs.* volume for FeCrTiSb quaternary Heusler alloy.

Table 1 Equilibrium lattice constant a_0, and ΔE ($\Delta E = E_{NM} - E_{FM}$) the total energy difference between NM and FM for the FeCrYZ (Y = Ti, Zr & Hf, Z = Sn & Sb) alloys

Alloys	Magnetic phase	a_0 (Å)	ΔE (Ry)
FeCrTiSn	NM	6.11	0.07
	FM	6.17	
FeCrZrSn	NM	6.35	0.04
	FM	6.38	
FeCrHfSn	NM	6.31	0.03
	FM	6.34	
FeCrTiSb	NM	6.08	0.02
	FM	6.12	
FeCrZrSb	NM	6.29	0.02
	FM	6.32	
FeCrHfSb	NM	6.27	0.00
	FM	6.29	

that the FM state is more stable when $\Delta E > 0$, whereas the NM state is more robust when $\Delta E = 0$. From Table 1, almost all alloys were stable in the FM state, except for the FeCrHfSb alloy which is stable in the NM state.

The elastic constants of solids link a crystal's mechanical and dynamic properties. Table 2 displays the computed C_{11}, C_{12}, and C_{44} elastic constants, along with the bulk modulus B, shear modulus G, Young's modulus E, B/G ratio, Cauchy pressure C_p, Poisson's ratio ν, and shear anisotropic factor A for FeCrYZ (Y = Ti, Zr, & Hf, Z = Sn & Sb) at ambient conditions. The angular behaviour of atomic bond formation in metals alloys can be described by Cauchy pressure $C_p = (C_{12} - C_{44})$. The negative Cauchy's pressure denotes brittleness, whereas the positive Cauchy's pressure denotes ductility. Table 2 shows that the calculated positive value C_p indicates that FeCrTiSn, FeCrTiSb and FeCrZrSb alloys are ductile by nature and the negative value C_p indicates that FeCrZrSn, FeCrHfSn and FeCrHfSb alloys are brittle in nature. The macroscopic mechanical properties of FeCrYZ (Y = Ti, Zr & Hf, Z = Sn & Sb) alloys, such as B, G, E, B/G ratio, and ν were computed using the given equations. The bulk modulus B of a material, which measures its resistance to volume change, is

$$B = \frac{1}{3}(C_{11} + 2C_{12}) \quad (1)$$

A material's stiffness and resistance to plastic deformation can be determined using its shear modulus (G), which is given by

$$G = \frac{1}{5}(C_{11} - C_{12} + 3C_{44}) \quad (2)$$

Young's modulus (E), mechanical properties, measures both stiffness or flexibility of solid materials, and Poisson's ratio (ν), a mechanical parameter, is particularly helpful for defining the malleability of materials (brittle or ductile) and defines the type of atomic bond formation in the particles, with a critical value of 0.26 (ref. 48) distinguishing between covalent and ionic bonding.

$$E = \frac{9BG}{(3B + G)} \quad (3)$$

$$\nu = \frac{3B - 2G}{2(3B + G)} \quad (4)$$

Pugh's[49] ratio, defined as B/G, is also used to explain the ductility and brittleness of an alloy. The material is brittle if B/G < 1.75 and Poisson's ratio (ν) < 0.26; else, it is ductile. The computed B/G ratio and Poisson's ratio (ν) in Table 2 reveal that FeCrTiSn, FeCrTiSb, and FeCrZrSb alloys are ductile, whereas FeCrZrSn, FeCrHfSn and FeCrHfSb alloys indicate their brittle nature. For the mechanical stability of cubic crystals, the following are the basic and sufficient requirements for the elastic constants.[50]

$$C_{11} > 0,\ C_{44} > 0,\ C_{11} - C_{12} > 0,\ C_{11} + 2C_{12} > 0 \quad (5)$$

The FeCrTiSn, FeCrTiSb, and FeCrZrSb alloys are elastically stable as indicated in Table 2 since predicted elastic constants satisfy the aforementioned constraints.

Anisotropic materials are those whose physical properties vary depending on their orientation. This is because the atomic densities in the crystal directions differ. The shear anisotropy factor calculates the degree of elastic anisotropy (A). The elastic isotropic material is represented by the value ($A = 1$), whereas the anisotropic properties are represented by ($A \neq 1$). The anisotropy factor for a cubic structure is written as follows in terms of elastic constants:

$$A = \frac{2C_{44}}{C_{11} - C_{12}} \quad (6)$$

Furthermore, we examine elastic anisotropy by computing the directional dependent shear modulus and Poisson's ratio,

Table 2 The calculated elastic constants (GPa), bulk modulus B (GPa), shear modulus G (GPa), Young's modulus E (GPa), B/G ratio, Cauchy pressure C_p (GPa), Poisson's ratio ν and shear anisotropic factor A for FeCrYZ (Y = Ti, Zr & Hf, Z = Sn & Sb) alloys at equilibrium conduction

Alloys	C_{11}	C_{12}	C_{44}	B	G	E	B/G	C_p	ν	A
FeCrTiSn	244.344	135.533	120.438	171.581	94.025	238.509	1.83	15.095	0.269	2.214
FeCrZrSn	271.911	103.695	208.624	159.802	158.82	357.891	1.00	−104.9	0.127	2.481
FeCrHfSn	411.154	73.155	198.619	186.672	186.772	420.181	0.99	−125.5	0.125	1.176
FeCrTiSb	239.928	162.758	63.027	188.166	53.251	145.981	3.54	99.731	0.371	1.634
FeCrZrSb	239.360	140.347	95.575	173.181	77.148	201.519	2.25	44.772	0.307	1.931
FeCrHfSb	409.137	72.087	174.676	184.589	172.216	394.089	1.08	−102.6	0.144	1.037

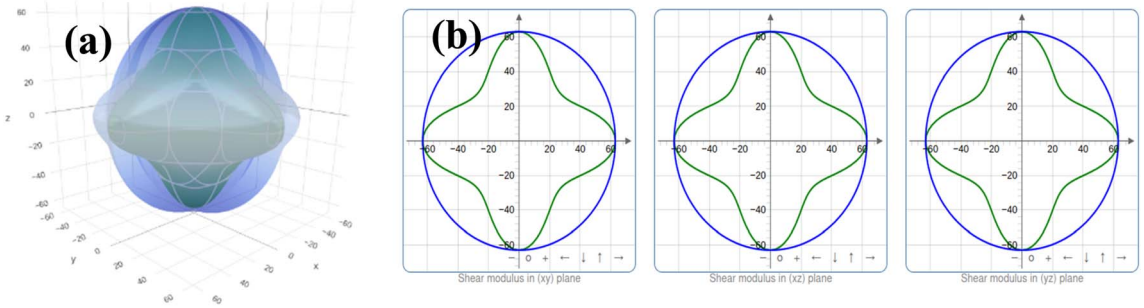

Fig. 2 Directional dependence shear modulus for FeCrTiSb in (a) 3D and (b) 2D.

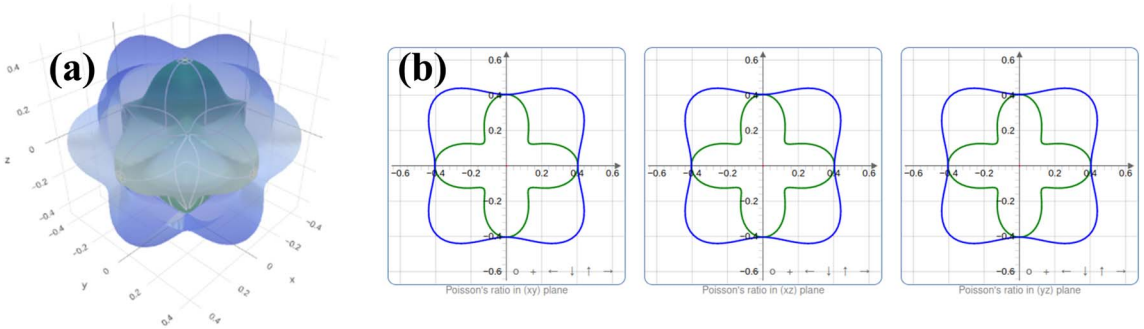

Fig. 3 Directional dependence Poisson's ratio for FeCrTiSb in (a) 3D and (b) 2D.

and the elastic tensor analysis (ELATE) code visualises their 2D projections and 3D surface constructions. For illustration, elastic anisotropy for FeCrTiSb are shown in Fig. 2 and 3. Table 2 clearly shows that FeCrYZ (Y = Ti, Zr & Hf, Z = Sn & Sb) alloys are classified as elastically anisotropic material.

Phonon dispersion

Using Quantum Espresso, phonon calculations are performed in two stages to explore the dynamic stability. The density functional perturbation theory (DFPT) is applied. First, the crystal structure was optimised with Quantum Espresso (a approach based on the plane-wave pseudopotential). The optimised results agreed well with the WIEN2K code. The phonon calculations were carried out on a 2 × 2 × 2 mesh in the phonon Brillouin zone. To the author's knowledge, phonon dispersion curves of FeCrYZ (Y = Ti, Zr, & Hf, Z = Sn & Sb) alloys have not yet been theoretically and experimentally examined. Fig. 4a and b illustrate the phonon dispersion, total and partial density of states (DOS) for FeCrTiSb. Positive frequencies are observed in the phonon mode, indicating that novel FeCrTiSn and FeCrTiSb are dynamically stable. There are three acoustical and nine optical sections for FeCrTiSn and FeCrTiSb the maximum acoustic phonon frequency are 136.57 cm^{-1} and 151.58 cm^{-1} respectively. A soft transverse

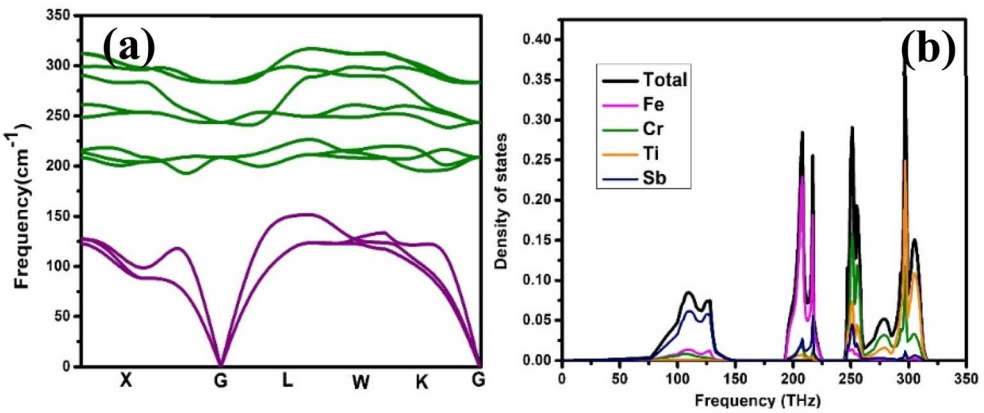

Fig. 4 (a) Phonon dispersion curve and (b) total and partial density of states (DOS) of FeCrTiSb.

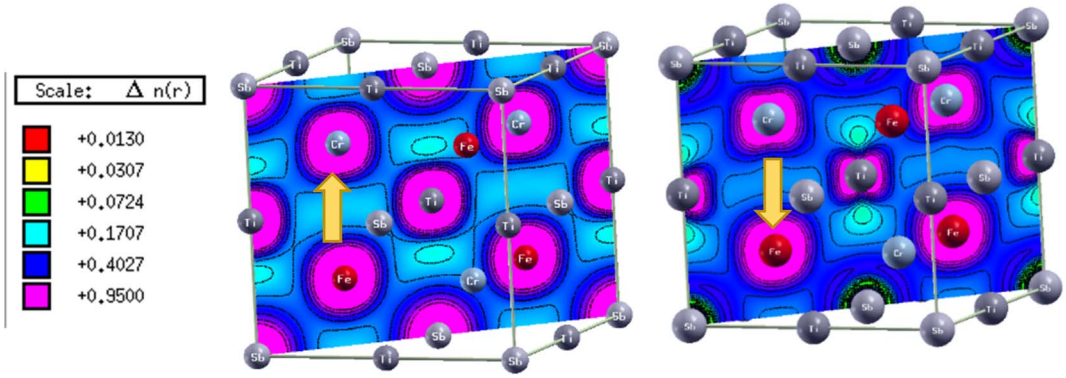

Fig. 5 Electronic charge density of contour plots FeCrTiSb for a majority and minority spin in (110) plane.

acoustic mode has been discovered for FeCrZrSn, FeCrZrSb, FeCrHfSn, and FeCrHfSb. In FeCrZrSn phonon becomes imaginary in the *X* and *L* direction, *X* and *K* in FeCrZrSb, *X* in FeCrHfSn, and *X* in FeCrHfSb alloy indicate that it is dynamically unstable. The results for FeCrTiSn, FeCrZrSn, FeCrHfSn, FeCrZrSb, and FeCrHfSb are shown in Fig. 1a–e, which can find in the ESI document.

Electronic charge density

The electronic charge density clearly depicts the type of chemical bonding and is commonly utilized in charge distributions Fig. 5 illustrates the charge density contours for both majority and minority spins in the (110) plane to forecast the chemical bond's nature in FeCrTiSb alloy. These contour planes show that the charge distributions of Fe and Sb are spherically symmetric, implying ionic bonding. The rest of the atoms have a distorted spherical charge distribution, implying electron sharing and the formation of covalent bonds. The charge density figure indicates that the nature of bonding in FeCrYZ (Y = Ti, Zr & Hf, Z = Sn & Sb) alloys are a combination of covalent and ionic, as well as polar covalent bonding is maintained in these crystal structures.

Electronic properties

The spin-polarized electronic band structure of quaternary Heusler alloys FeCrYZ (Y = Ti, Zr, & Hf, Z = Sn & Sb) calculated within generalized gradient approximation (GGA) with modified Becke–Johnson (mBJ) exchange–correlation potentials were plotted in the Brillouin zone along selected high symmetry lines. The band structure for FeCrTiSb in the ferromagnetic state at its equilibrium volume is illustrated in Fig. 6, the minority-spin bands cross the Fermi level and show metallic nature. While the majority spin has an indirect energy band gap near the Fermi level, resulting in an HM ferromagnetic alloy with 100% spin-polarized conduction electrons. The mBJ approach is used with GGA to provide a precise band structure because the GGA approach undervalues the energy band gap. For FeCrTiSn, FeCrZrSn, FeCrHfSn and FeCrZrSb alloys, the overall profile of the band structure is the same. Whereas for FeCrHfSb, there is no spin-polarization of energy levels around the E_F, indicating that it is non-magnetic. FeCrYZ (Y = Ti & Zr, Z = Sn & Sb) and FeCrHfSn alloys can be considered excellent candidates for spintronics applications due to its wider spin-flip band gaps and robust half-metallicity.

To further investigate the electronic structures of FeCrYZ (Y = Ti, Zr, & Hf, Z = Sn & Sb) alloys, the total density of states (TDOS), and partial density of states (PDOS) were estimated at their respective equilibrium lattice parameters. Fig. 7 and 8 show the plotted TDOS and PDOS of FeCrTiSb computed using the GGA and mBJ approximations. PDOS provides information on the energy states that exist in each energy interval. The Cr-3d states, Fe-3d states, Zr-4d states, and Hf-5d states made the major contribution to the DOS near the Fermi level. The significance of 5p-like states of Sn or Sb is very small near the E_F. The spin polarization (*P*) at the Fermi level of FeCrYZ (Y = Ti & Zr, Z = Sn & Sb) and FeCrHfSn alloys are examined using the estimated TDOS using the equation:

$$P = \frac{n\uparrow(E_F) - n\downarrow(E_F)}{n\uparrow(E_F) + n\downarrow(E_F)} \times 100\% \quad (7)$$

where $n\uparrow$ (E_F) and $n\downarrow$ (E_F) denote the spin-dependent DOS surrounding the Fermi level. FeCrYZ (Y = Ti & Zr, Z = Sn & Sb) and FeCrHfSn alloys exhibit 100% *P* near the Fermi level, implying half-metallic behaviour.

Origin of half metallic gap

The gaps in half-metallic materials are formed through charge transfer, covalent bonding, or d–d hybridization. In Heusler alloys (HA), d–d hybridization predominates and is consequently responsible for the energy band gap. Hence, the presence of a gap in FeCrYSn (Y = Ti, Zr & Hf), FeCrTiSb and FeCrZrSb can be inferred by illustrating potential d–d hybridization, as depicted in Fig. 9 for FeCrTiSb alloy. The main group Sb-5p states are most electronegative of all components and require three electrons to fulfill its octet, which are contributed by 3d states of Fe and Ti consequence, it contributes the least to band structure just at the Fermi level, as demonstrated by the Sb-p state in PDOS. First, we'll discuss Fe–Ti hybridization once s-electrons are removed, Ti-d has three electrons and Fe-d has six electrons in transition metals, the Jahn–Teller distortion eliminates the degeneracy of d-orbitals to reduce energy. The d-states orbital is divided into doubly degenerate states $2e_g$ ($d_{x^2-y^2}$, d_{z^2}) and triply degenerate

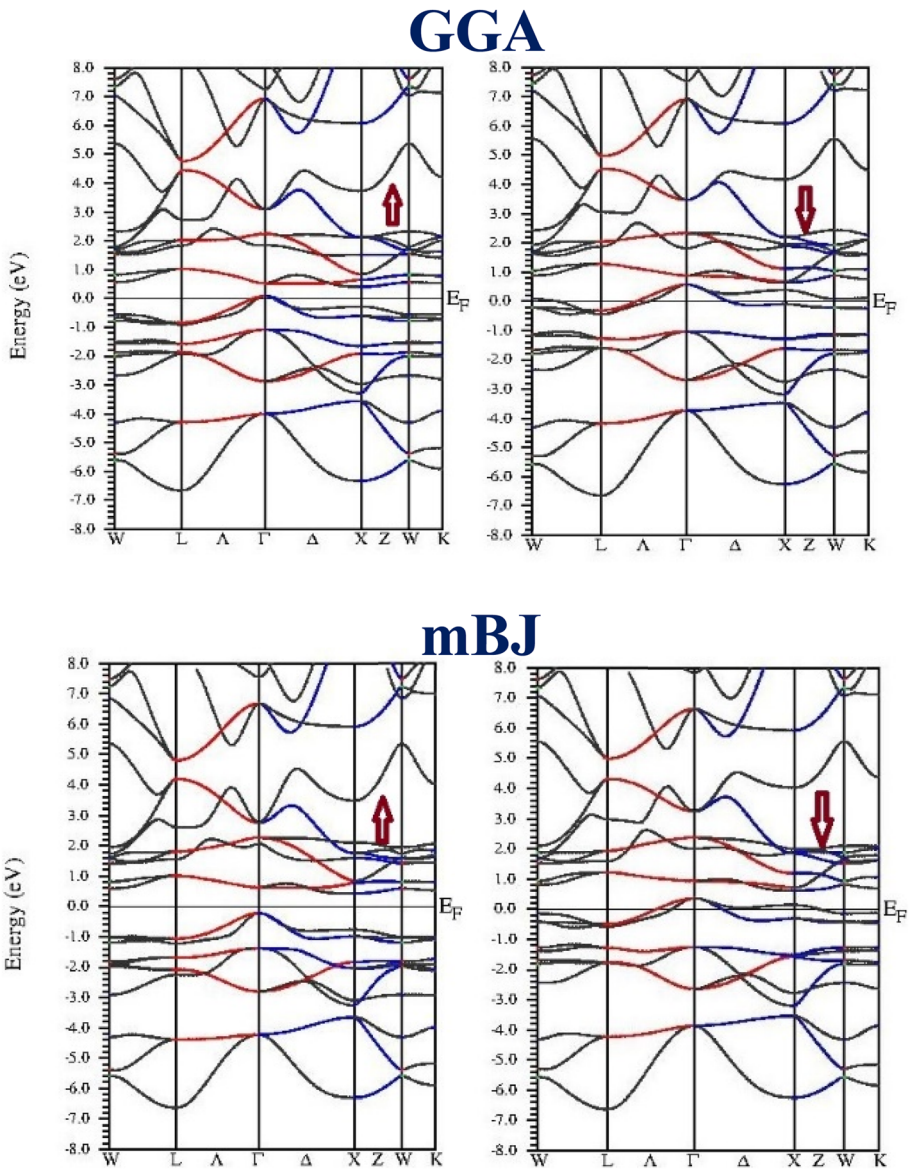

Fig. 6 Electronic band structure of FeCrTiSb quaternary Heusler with GGA and mBJ in majority and minority spin.

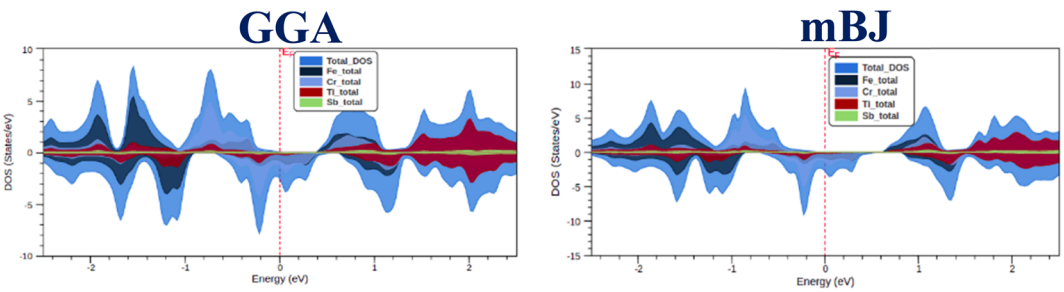

Fig. 7 The total density of states (TDOS) of FeCrTiSb with GGA and mBJ.

states $3t_{2g}$ (d_{xy}, d_{yz}, d_{zx}). This hybridization generates both bonding ($2e_g$ and $3t_{2g}$) and anti-bonding ($2e_u$ and $3t_{1u}$) states. Further hybridization happens when tetrahedral bonding d-states of Fe–Ti interact with the d-states of Cr that have tetrahedral symmetry. Non-bonding $2e_u$ and $3t_{1u}$ states have no interaction with Cr-d states because of different symmetry. The E_F is situated between the states of $2e_u$ and $3t_{1u}$. In this study, the properties of alloys are determined by strong d–d hybridization.

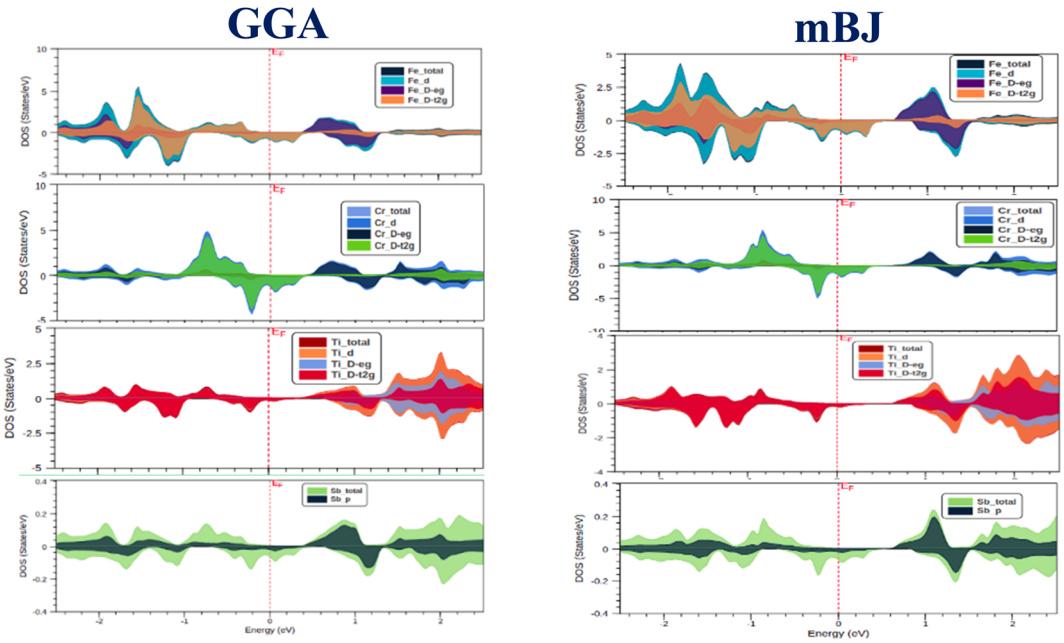

Fig. 8 Partial density of states (PDOS) of FeCrTiSb with modified Becke–Johnson (mBJ).

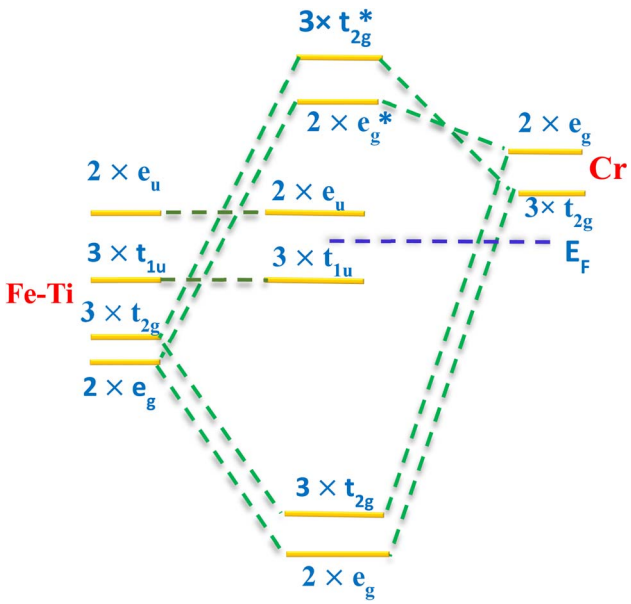

Fig. 9 The d–d hybridizations between the majority spin of Cr, Fe, and Ti transition metals of FeCrTiSb quaternary Heusler alloy is depicted schematically.

Several other studies have shown that the sp atoms have a drastic impact on the electronic properties of HA. As a result, we may say that HA parameters are acquired by p–d and d–d hybridizations.

Magnetic properties

The magnetic nature of a substance can be explained using the total magnetic moment. Table 3 displays the total, individual, interstitial magnetic moments, and band gap of FeCrYZ (X = Ti, Zr & Hf, Z = Sn & Sb) alloys using the GGA and mBJ potential. FeCrYZ (Y = Ti & Zr, Z = Sn & Sb) and FeCrHfSn alloys satisfy the Slater–Pauling formula MT = $ZT - 24$ and have excellent half-metallic properties with total integer magnetic moments of $2.0\mu_B$ and $1.0\mu_B$ respectively. It is evident from Table 3 that Cr atoms make a significant contribution to the overall magnetic moment. Interstitial has a value close to zero, this indicates that there is very little charge leak into the alloys' interstitial regions. Both GGA and mBJ exchange–correlation produce almost the same magnetic moments. The contributions of Ti/Zr/Hf and Sn/Sb atoms to the magnetic moment are negligible in comparison to Cr and Fe atoms. Indicated by their negative magnetic moments, the Ti/Zr/Hf and Sn/Sb atoms' spin magnetic moments are antiparallel to those of the Fe and Cr atoms.

Thermoelectric properties

For efficient TE materials, high values of S and σ/τ with low κ_e/τ are expected. When these values are optimal, the dimensionless ZT may be optimized. However, these parameters are connected to each other. To gain insight into the TE performance of quaternary Heusler alloys, we compute the S, σ/τ, κ_e/τ, power factor (PF), and ZT of FeCrYZ (Y = Ti, Zr, and Hf, Z = Sn and Sb) alloys. Electronic transport properties are examined using Boltzmann theory. Because the PBE function is known to underestimate the gap between the bands, the thermoelectric properties were estimated using the TB-mBJ function. The transport characteristics are evaluated across a temperature range of 100–900 K, and the results were shown in Table 4.

The Seebeck coefficient (S), commonly known as thermopower, quantifies the material's ability to transform a temperature differential into voltage. The Seebeck coefficient (S) of FeCrYZ (Y = Ti, Zr, and Hf, Z = Sn and Sb) alloys is depicted in

Table 3 The calculated partial, interstitial, total magnetic moment, band gap and half metallic E_{HM} gap for FeCrYZ (Y = Ti, Zr & Hf, Z = Sn & Sb) alloys

Alloys		Fe (μ_B)	Cr (μ_B)	Ti/Zr/Hf (μ_B)	Sn/Sb (μ_B)	Int. (μ_B)	Total (μ_B)	E_g (eV)	E_{HM} (eV)
FeCrTiSn	GGA mBJ	0.51	1.85	−0.37	−0.03	0.03	1.99	1.25	0.05
		0.51	1.81	−0.31	−0.02	0.01	2.00	1.42	
FeCrZrSn	GGA mBJ	0.33	1.67	−0.10	−0.02	0.11	1.99	0.26	0.41
		0.33	1.70	−0.10	−0.02	0.09	2.00	0.88	
FeCrHfSn	GGA mBJ	0.39	1.60	−0.07	−0.0 1	0.09	2.00	0.48	0.04
		0.39	1.60	−0.07	−0.01	0.09	2.00	0.62	
FeCrTiSb	GGA mBJ	0.49	0.73	−0.26	−0.00	−0.01	0.99	0.93	0.10
		0.51	0.79	−0.30	−0.00	−0.00	1.00	1.16	
FeCrZrSb	GGA mBJ	0.33	0.67	−0.04	−0.00	0.04	1.00	0.30	0.69
		0.35	0.80	−0.11	−0.01	0.03	1.00	0.92	

Table 4 The calculated Seebeck coefficient S, electrical conductivity σ/τ, thermal conductivity κ_e/τ, power factor $S^2\sigma$, and figure of merit ZT for FeCrYZ (Y = Ti, Zr & Hf, Z = Sn & Sb) alloys

Alloys	T (K)	Type	S (μV K)	σ/τ 10^{19} Ω^{-1} m^{-1} s^{-1}	κ_e/τ (10^{14} W m^{-1} K^{-1} s^{-1})	$S^2\sigma/\tau$ (10^{11} W m^{-1} K^{-1})	ZT
FeCrTiSn	300	p	14.2	3.19	0.42	6.61	0.47
	900	n	−1.78	11.41	9.65	0.03	0.01
FeCrZrSn	300	n	−33.6	2.19	0.85	23.1	0.88
	900	n	−21.99	18.43	11.53	87.6	0.69
FeCrHfSn	300	n	−42.3	0.21	0.19	0.42	0.61
	900	n	−21.75	10.49	11.19	50.9	0.39
FeCrTiSb	300	n	−110.1	2.42	16.1	29.3	0.55
	900	n	−161.22	4.14	57.27	107.6	1.79
FeCrZrSb	300	n	−49.6	7.89	52.9	18.4	0.11
	900	n	−92.01	7.78	103.91	65.81	0.61
FeCrHfSb	300	n	−54.3	6.04	42.8	17.8	0.13
	900	n	−111.00	6.79	99.39	83.35	0.86

Fig. 10(a) and 11(a) and the values are listed in Table 4. The Seebeck coefficient is calculated using the electronic density of states (DOS) obtained from the first-principles calculation. Seebeck coefficient for FeCrTiSn alloy reduces significantly around 600 K, and additional temperature increase caused a sign shift from p-type to n-type. In mild temperatures of 900 K, both p-type and n-type contributions cancel each other leading to a low S as shown in Fig. 10(a). Whereas S of FeCrZrSn and FeCrHfSn alloys show a maximum at 300 K given in Table 4, it decreases as temperature increases. Thus, decreasing nature of Seebeck coefficients, particularly in semiconducting materials, is caused by an increase in carrier concentration, producing more electron–hole pairs, causing more scattering effects, leading to a decrease in the S. A negative S indicates that the alloys are n-type, and the majority carriers are electrons. Fig. 11(a) depicts Seebeck coefficients of FeCrYSb (Y = Ti, Zr & Hf) alloys. At 300 K S increase with increasing temperature and reach a maximum at 900 K given in Table 4. The highest values of the S are according to the band degeneracy, in accordance with which the effective mass directly relates to band degeneration ($m^* = N_V^{2/3} m_b^*$) here N_V and m_b^* denote the effective mass related to a single valley degeneracy that can increase. Likewise, the effect of the S on the effective mass is illustrated by the Mott relation shown below in eqn (8). As a result, the increase in S is due to the decrease of carrier concentration.

$$S = \frac{8\pi^2 {\kappa_B}^2}{3eh^2} m^* T \left(\frac{\pi}{3n}\right)^{2/3} \quad (8)$$

where m^* represents the effective mass, n represents the carrier concentrations, κ_B represents the Boltzmann's constant, e represents the electronic charge, h represents Planck's constant, and T represents the temperature.

The electrical conductivity (σ/τ) of FeCrYZ (Y = Ti, Zr, and Hf, Z = Sn and Sb) alloys are depicted in Fig. 10(b) and 11(b) and the values are given in Table 4. It shows that the electrical conductivity rises as the temperature rises and peaks at 900 K the high electrical conductivity is induced by the high density of charge carriers, which is a common trend in semiconductor materials. The electronic thermal conductivity (κ_e/τ) of FeCrYZ (Y = Ti, Zr, and Hf, Z = Sn and Sb) alloys are plotted in Fig. 10(c) and 11(c) and values are given in Table 4. Wiedemann–Franz law $\kappa_e = L\sigma T$ relates thermal conductivity with electrical conductivity. Thus, it is logical to expect thermal conductivity to behave similarly to electrical conductivity. High thermoelectric efficiency suggests that κ is dominated by electrons within a band. Thermal conductivity rises as temperature rises and reaches its peak at 900 K. The power factor (PF) of FeCrYZ (Y = Ti, Zr, and Hf, Z = Sn and Sb) alloys are depicted in Fig. 10(d) and 11(d) and values are given in Table 4. The S and σ/τ were used to determine the PF of a material which measures

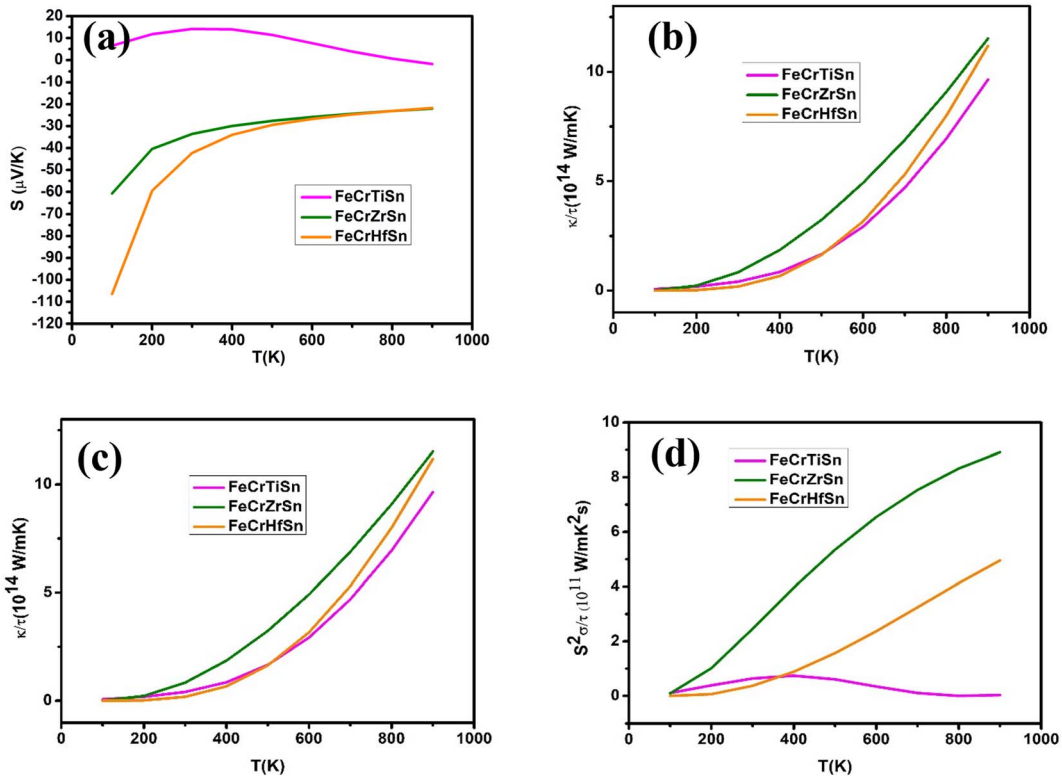

Fig. 10 Calculated (a) Seebeck coefficient S, (b) electrical conductivity σ/τ, (c) thermal conductivity κ_e/τ, (d) power factor $S^2\sigma$ as a function of temperature for FeCrYSn (Y = Ti, Zr & Hf).

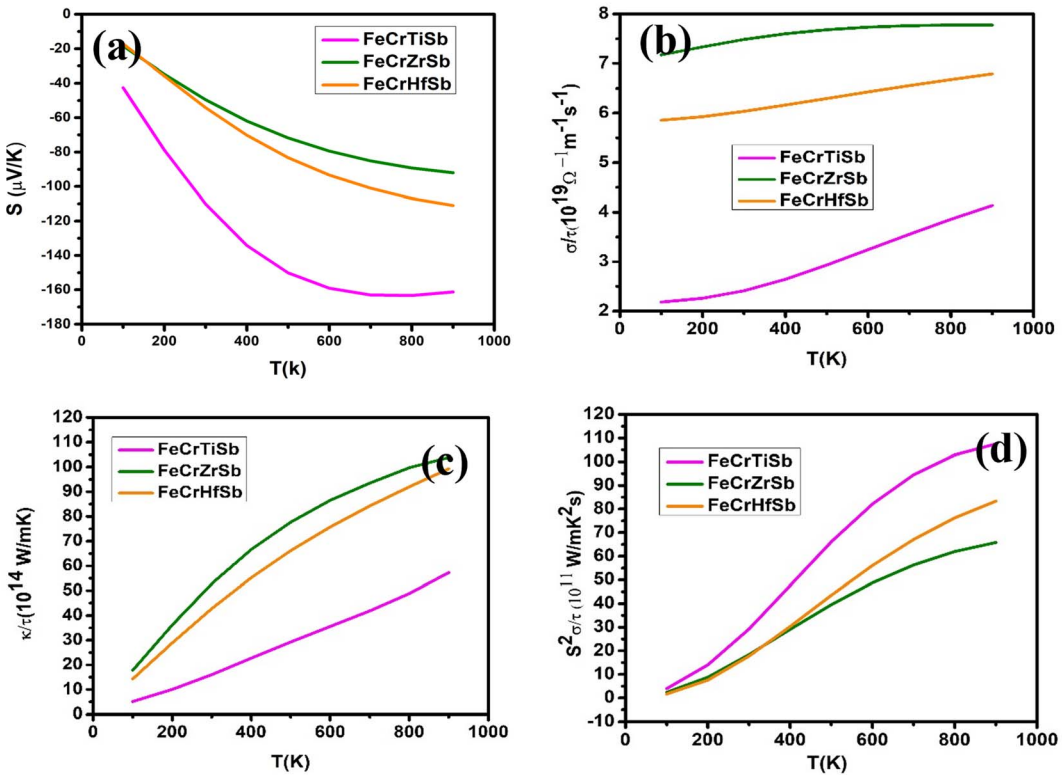

Fig. 11 Calculated (a) Seebeck coefficient S, (b) electrical conductivity σ/τ, (c) thermal conductivity κ_e/τ, (d) power factor $S^2\sigma$ as a function of temperature for FeCrYSb (Y = Ti, Zr & Hf).

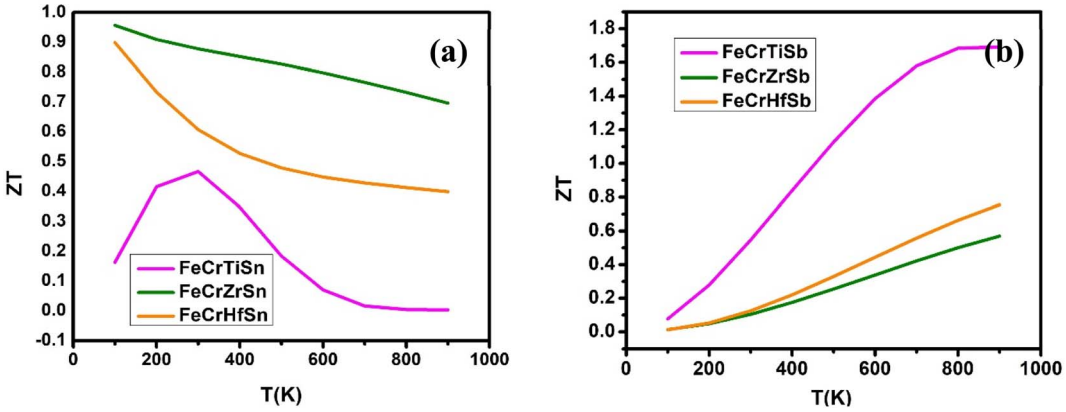

Fig. 12 Calculated figure of merit *ZT* as a function of temperature for (a) FeCrYSn (Y = Ti, Zr & Hf) and (b) FeCrYSb (Y = Ti, Zr & Hf).

a material's efficiency. The study reveals that the PF rises as temperature rises, maximum at 900 K.

Only the electronic part of κ_e/τ was included while evaluating the *ZT* in this case. The *ZT* of FeCrYZ (Y = Ti, Zr, and Hf, Z = Sn & Sb) alloys are depicted in Fig. 12(a) and (b). In Fig. 12(a) among FeCrYSn (Y = Ti, Zr, and Hf) alloys, FeCrTiSn has the lowest *ZT* value of 0.01. This is because FeCrTiSn has a lower Seebeck coefficient than other alloys. Furthermore, the high electrical conductivity of FeCrTiSn might result in a high electronic contribution to thermal conductivity, which substantially reduces the value of *ZT*. The maximum *ZT* values are attained by FeCrZrSn and FeCrHfSn at temperatures of about 100 K and whereas for FeCrTiSn is around 300 K. Fig. 12(b) shows FeCrTiSb has a maximum *ZT* that is close to 1.79 at a higher temperature of 900 K. Table 4 shows the *ZT* value at 900 K. As *S*, σ/τ and *ZT* increase with temperature, FeCrTiSb alloys could be employed in thermoelectric technology.

Optical properties

The optical properties of FeCrYZ (Y = Ti, Zr, & Hf, Z = Sn & Sb) alloys were examined, using the FP-LAPW technique and modified Becke–Johnson (mBJ). The analysis of optical properties focused on energy absorption or dissipation using the Kramer–Kronig relation ($\varepsilon(\omega)$ denotes the dielectric function), which is described as

$$\varepsilon(\omega) = \varepsilon_1(\omega) + i\varepsilon_2(\omega) \quad (9)$$

where $\varepsilon_1(\omega)$ is the real part of the dielectric function which represents the dispersion relation of electromagnetic waves, and $i\varepsilon_2(\omega)$ is the imaginary part of the dielectric function that represents the difference between the wave functions of occupied and unoccupied levels as calculated by the momentum matrix element.

From the Drude model, intraband transitions contribute to the infrared absorption by free electrons. As can be seen, the real parts $\varepsilon_1(\omega)$ and imaginary parts $i\varepsilon_2(\omega)$ for FeCrYZ (Y = Ti, Zr, and Hf, Z = Sn & Sb) in which the highly free electron charge carriers are found to be present in the materials indicates the intraband transitions. Fig. 13(a) and 14(a) indicates the real part of $\varepsilon_1(\omega)$, for FeCrYZ (Y = Ti, Zr, and Hf, Z = Sn & Sb) alloys with respect to photon energy ranging from 0–14 eV. The real part of FeCrTiSn shows that it has a high polarisation value of 42, whereas FeCrZrSn has 26, FeCrTiSb has 24, FeCrZrSb has 4, FeCrHfSb has 5. Furthermore, we see that real parts decline with energy from 0 to 3 eV and nearly vanish at high energies. Whereas the real part of the static dielectric function shifts to 13.5 eV for FeCrHfSn alloy; this suggests a negative value of $\varepsilon_1(\omega)$, in the energy band 0–0.3 eV demonstrating the loss of light transit of FeCrHfSn alloy. We see that $\varepsilon_1(\omega)$ in the 0.36 eV for FeCrHfSn. Where $\varepsilon_1(\omega) = 0$ occurs, the alloy does not react to incident light, owing to plasmon oscillations. Fig. 13(b) and 14(b) indicates the imaginary part of $\varepsilon_2(\omega)$, for FeCrYZ (Y = Ti, Zr, and Hf, Z = Sn & Sb) alloys with respect to photon energy ranging from 0–14 eV. The majority of transit occurred in the infrared region (energies less than 0.1 eV), implying that these alloys are metals. In other words, the electrons are transferred intraband due to the low energy content of incident photons. However, at energy 0.1 eV, the $\varepsilon_2(\omega)$ curves of all alloys rapidly decrease, which again indicates plasmon oscillation.

Fig. 13(c) and 14(c) depicts absorption coefficient $I(\omega)$ of FeCrYZ (Y = Ti, Zr, and Hf, Z = Sn & Sb) alloys with respect to photon energy ranging from 0 to 14 eV. As expected, because these alloys are metals, absorption begins at extremely low photon energies. In the visible range, the absorption curve quickly ascends and maxima at 2 eV. A significant portion of the light received in the infrared (IR) and visible spectrums significantly contributed to the electron transition. The conductivity decreases dramatically in the IR range, yet the absorption approaches saturated in the UV limit. Fig. 13(d) and 14(d) depict reflectivity $R(\omega)$ of FeCrYZ (Y = Ti, Zr, & Hf, Z = Sn & Sb) alloys with respect to photon energy ranging from 0 to 14 eV. The reflective coefficient of a material is calculated by the sum of wave energy reflected to wave energy incident at the material's surface. All these alloys have a strong metallic character, with a static reflection index greater than 95%. However, during plasmonic oscillation, this value drops to 40%. Notably, for all graphs in the IR, visible, and UV ranges, FeCrTiSn and FeCrTiSb respond more strongly to incident photons than FeCrYZ (Y = Zr & Hf, Z = Sn & Sb).

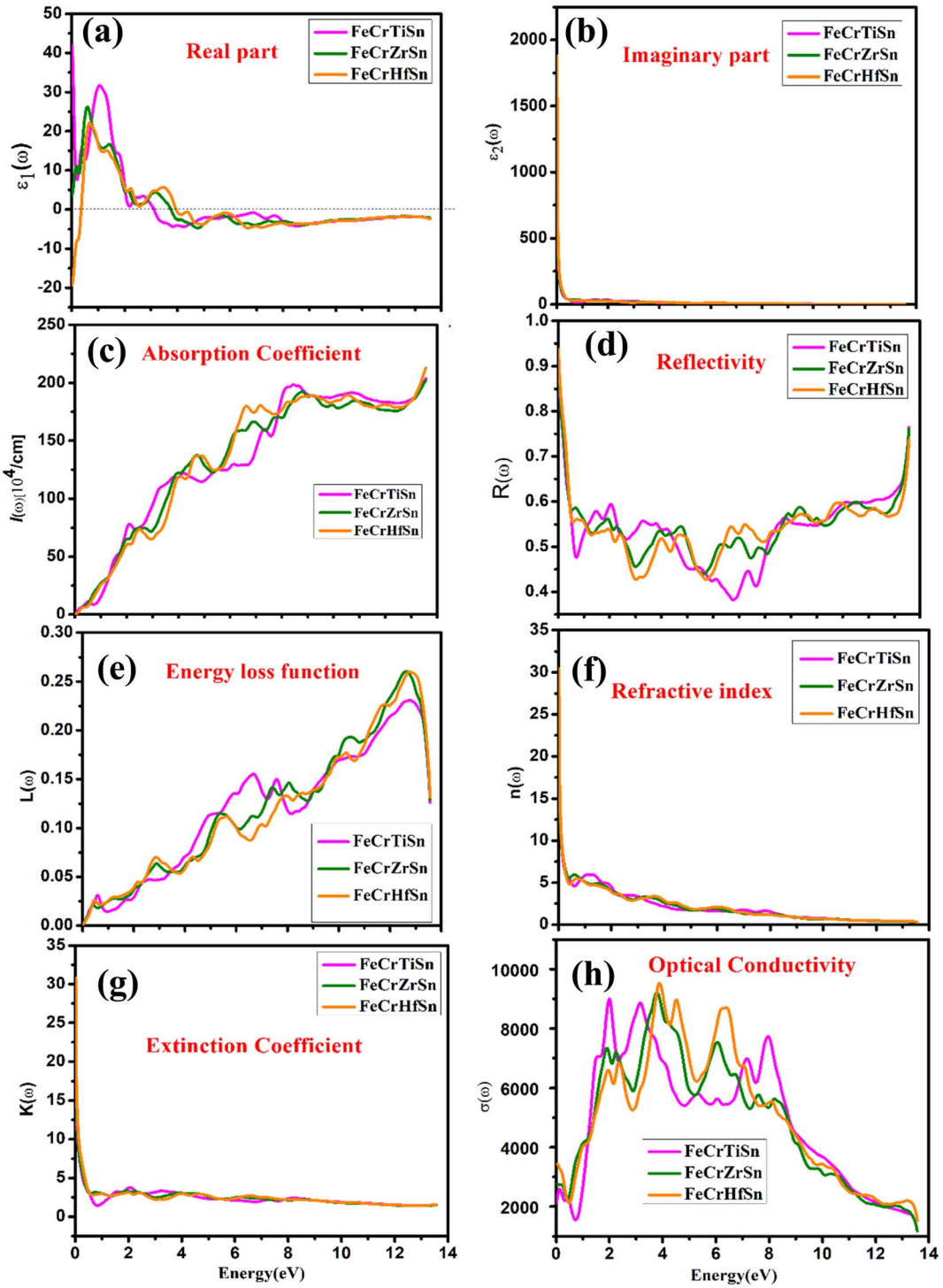

Fig. 13 (a) Real $\varepsilon_1(\omega)$, (b) imaginary $\varepsilon_2(\omega)$, (c) absorption coefficient $I(\omega)$, (d) reflectivity $R(\omega)$, (e) energy loss function $L(\omega)$, (f) refractive index $n(\omega)$, (g) extinction coefficient $K(\omega)$, and (h) optical conductivity $\sigma(\omega)$ for FeCrYSn (Y = Ti, Zr & Hf) QHA.

Fig. 13(e) and 14(e) depicts energy loss function $L(\omega)$ of FeCrYZ (Y = Ti, Zr, & Hf, Z = Sn & Sb) alloys with respect to photon energy ranging from 0 to 14 eV. Excitations caused by fast-moving electrons and optical spectra created by them are defined by incident photon energy. The $L(\omega)$ is caused by electron excitations, which happen when a fast electron passes through a substance energy loss increases as incident photon energy increases. Most energy loss in the ultraviolet region, around 13.5 eV.

Fig. 13(f) and 14(f) depicts refractive index $n(\omega)$ of FeCrYZ (Y = Ti, Zr, and Hf, Z = Sn & Sb) alloys with respect to photon energy ranging from 0 to 14 eV. The refractive index is significant when trying to figure out how light interacts with matter. It also gives information on phase velocity, which is defined by the

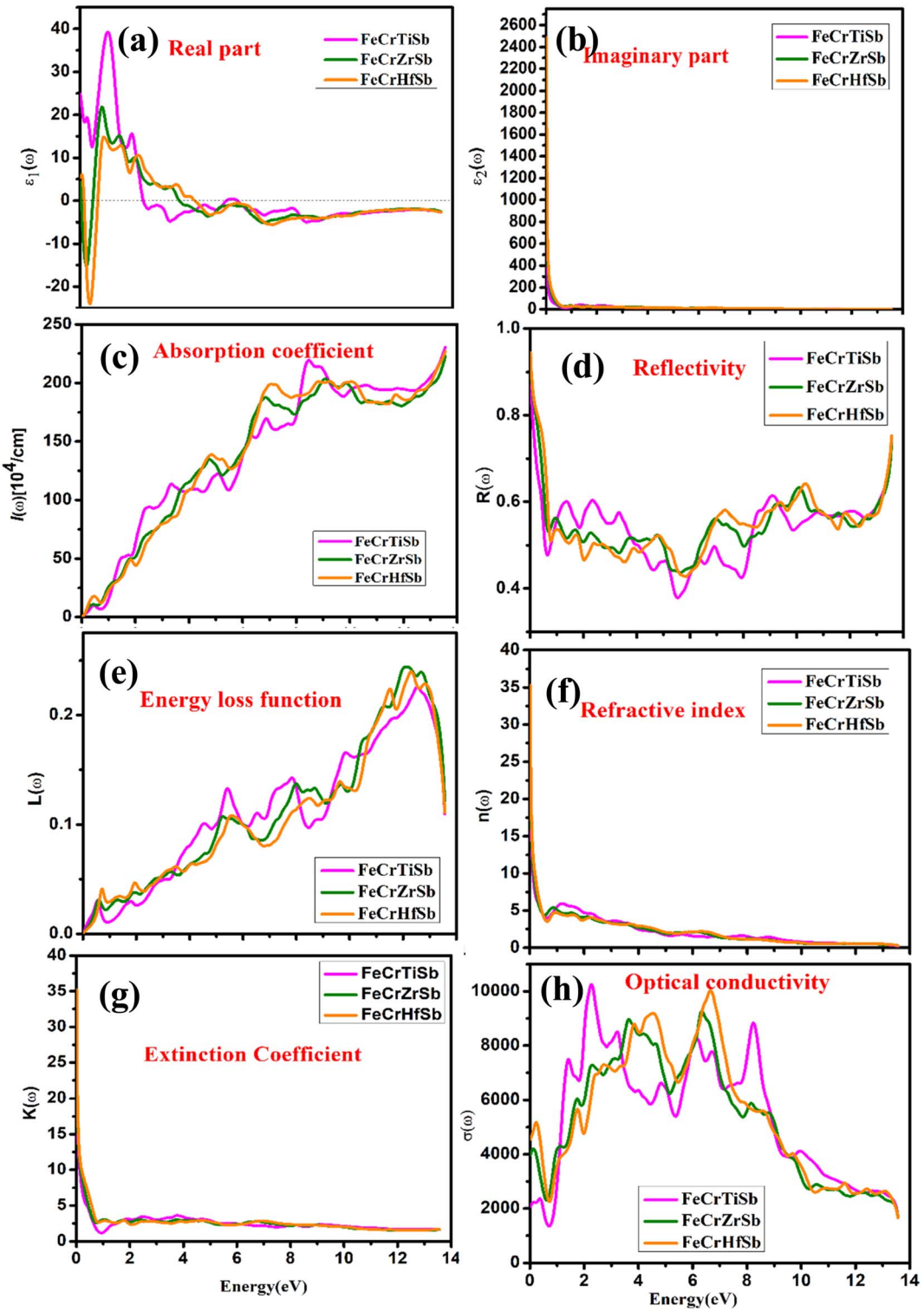

Fig. 14 (a) Real $\varepsilon_1(\omega)$, (b) imaginary $\varepsilon_2(\omega)$, (c) absorption coefficient $I(\omega)$, (d) reflectivity $R(\omega)$, (e) energy loss function $L(\omega)$, (f) refractive index $n(\omega)$, (g) extinction coefficient $K(\omega)$, and (h) optical conductivity $\sigma(\omega)$ for FeCrYSb (Y = Ti, Zr & Hf) QHA.

dielectric function's real portion. We see a decreasing relationship between $n(\omega)$ and photon energy. Peak values at zero energy are calculated to be 23.7, 27.5, 30.9, 29.4, 32.9, and 35.3 for FeCrTiSn, FeCrZrSn, FeCrHfSn, FeCrTiSb, FeCrTiSb, FeCrZrSb, and FeCrHfSb respectively.

Fig. 13(g) and 14(g) depicts extinction coefficient $K(\omega)$ of FeCrYZ (Y = Ti, Zr, and Hf, Z = Sn & Sb) alloys with respect to photon energy ranging from 0 to 14 eV. Light absorption by matter is measured by the extinction coefficient. The metallic nature of the material shows that the maximum extinction

coefficient occurs in the infrared and at the zero-energy range. However, as the incident photon's energy increases, the quantity of extinction coefficient rapidly decrease to the range of 1 eV and then continues to decrease.

Fig. 13(h) and 14(h) depicts optical conductivity $\sigma(\omega)$ of FeCrYZ (Y = Ti, Zr, & Hf, Z = Sn & Sb) alloys with respect to photon energy ranging from 0 to 14 eV. FeCrYZ (Y = Ti, Zr, & Hf, Z = Sn & Sb) are ideal for optoelectronic applications due to their high absorption coefficients and outstanding visible-range optical conductivities. The first peak occurs in the infrared range, implying that they could be employed as infrared detectors and sensors. The following peaks are in the ultraviolet and above region, which makes them suitable for UV device applications.

Conclusion

Full-potential linearized augmented plane wave (FP-LAPW) approach in the DFT was used to explore the structural, mechanical, electrical, magnetic, thermal, and optical properties of unique FeCrYZ (Y = Ti, Zr & Hf, Z = Sn & Sb) alloys that were predicted theoretically. Except for FeCrHfSb, all of the alloys are discovered to have stable HM ferromagnetic ground states during the energy minimization process, to total magnetic moments of $1.00\mu_B$, and $2.00\mu_B$ respectively obeying the Slater–Pauling law. Based on phonon dispersion curves FeCrTiSn, FeCrTiSb and FeCrZrSb are stable. At 900 K, the calculated *ZT* for FeCrTiSb is 1.76, FeCrZrSb is 0.61, and FeCrHfSb is 0.86. Optical spectra reveal that absorption occurs in the visible and near ultraviolet ranges of the spectra. According to current research, a narrow band gap, spin polarisation, and high *ZT* values are all excellent candidates for spintronics and thermoelectric applications. We believe that our findings, indicating the potential of novel FeCrTiSb alloy as promising spintronics, thermoelectric, and optoelectronics material, will motivate and promote experimenters to investigate these materials.

Conflicts of interest

There are no conflicts to declare.

References

1 J. S. Moodera, L. R. Kinder, T. M. Wong and R. Meservey, Large Magnetoresistance at Room Temperature in Ferromagnetic Thin Film Tunnel Junctions, *Phys. Rev. Lett.*, 1995, **74**(16), 3273.
2 G. Binasch, P. Grünberg, F. Saurenbach and W. Zinn, Enhanced magnetoresistance in layered magnetic structures with antiferromagnetic interlayer exchange, *Phys. Rev. B: Condens. Matter Mater. Phys.*, 1989, **39**, 4828.
3 S. A. Wolf, D. D. Awschalom, D. M. Treger, *et al.*, Spintronics: A Spin-Based Electronics Vision for the Future, *Science*, 2001, **294**, 1488.
4 J. Arreguin-Zavala, D. Vasilevskiy, *et al.*, Microwave Sintering of Bi2Te3- and PbTe-Based Alloys: Structure and Thermoelectric Properties, *J. Electron. Mater.*, 2013, **42**, 1992.
5 S. A. Khandy and J.-D. Chai, Thermoelectric properties, phonon, and mechanical stability of new half-metallic quaternary Heusler alloys: FeRhCrZ (Z = Si and Ge), *J. Appl. Phys.*, 2020, **127**, 165102.
6 M. Zeeshan, T. Nautiyal, *et al.*, FeTaSb and FeMnTiSb as promising thermoelectric materials: an *ab initio* approach, *Phys. Rev. Mater.*, 2018, **2**, 065407.
7 R. Dhakal, S. Nepal, *et al.*, Prediction of half-metallicity and spin-gapless semiconducting behavior in the new series of FeCr-based quaternary Heusler alloys: an Ab initio study, *J. Alloys Compd.*, 2021, **882**, 160500.
8 E. Pakizeh, J. Jalilian and M. Mohammadi, Electronic, optical and thermoelectric properties of Fe_2ZrP compound determined via first-principles calculations, *RSC Adv.*, 2019, **9**, 25900–25911.
9 A. Jazideh, A. Boochani and B. A. Nia, Half-metallic, magneto-optic, and thermoelectric properties of CoRuVZ (Z=Al, Ga), *Phys. Lett. A*, 2021, **414**, 127622.
10 S. Laghzaoui, A. F. Lamrani, R. A. Laamara, *et al.*, Realization of half-metal antiferromagnetic (HM-AFM) behaviour in double perovskite Sr_2CrReO_6 on substitution of Tc at Cr site: promising material for optoelectronics and thermoelectric applications via DFT framework, *Inorg. Chem. Commun.*, 2022, **146**, 110172.
11 S. Haid, W. Benstaali, A. Abbad, *et al.*, Thermoelectric, Structural, Optoelectronic and Magnetic properties of double perovskite Sr_2CrTaO_6: first principle Study, *Mater. Sci. Eng., B*, 2019, **245**, 68–74.
12 N. U. Khan, Abdullah, U. A. Khan, *et al.*, Investigation of structural, optoelectronic and thermoelectric properties of titanium based chloro-perovskites $XTiCl_3$ (X = Rb, Cs): a first-principles calculations, *RSC Adv.*, 2023, **13**, 6199–6209.
13 M. Singh, H. S. Saini, *et al.*, Electronic structure, magnetism and robust half-metallicity of new quaternary Heusler alloy FeCrMnSb, *J. Alloys Compd.*, 2013, **580**, 201–204.
14 K. M. Katubi, M. Zafar, *et al.*, Structural, elastic, thermodynamic, electronic and magnetic characteristics of FeNbScZ (Z = Al, Ga, Ge, Si) Heusler alloys: a DFT study, *Phys. B*, 2023, **650**, 414550.
15 K. Chinnadurai and B. Natesan, First principles calculations of 3d-4d transition metal based LiMgPdSn-type FeCrRuZ (Z = Al, Ga, In, Si) equiatomic quaternary Heusler alloys, *Comput. Mater. Sci.*, 2021, **188**, 110116.
16 S. A. Khandy, I. Islam, D. C. Gupta, *et al.*, A case study of Fe_2TaZ (Z = Al, Ga, In) Heusler alloys: hunt for half-metallic behavior and thermoelectricity, *RSC Adv.*, 2018, **8**, 40996.
17 B. Xu, X. F. Li, G. Q. Yu, J. Zhang, S. S. Ma, Y. S. Wang and L. Yi, *J. Alloys Compd.*, 2013, **565**, 22–28.
18 H. Luo, G. Liu, *et al.*, Half-metallicity in Fe-based Heusler alloys Fe_2TiZ (Z = Ga, Ge, As, In, Sn and Sb), *J. Magn. Magn. Mater.*, 2012, **324**, 3295–3299.
19 I. H. Bhat, T. M. Bhat and D. C. Gupta, Magneto-electronic and thermoelectric properties of some Fe-based Heusler alloys, *J. Phys. Chem. Solids*, 2018, **119**, 251.
20 M. Benidris, Z. Aziz, *et al.*, Electronic structure, thermoelectric, mechanical and phonon properties of full-

Heusler alloy (Fe_2CrSb): a first-principles study, *Bull. Mater. Sci.*, 2021, **44**, 221.

21 S. A. Khandy, I. Islam, D. C. Gupta, *et al.*, A case study of Fe2TaZ (Z = Al, Ga, In) Heusler alloys: hunt for half-metallic behavior and thermoelectricity, *RSC Adv.*, 2018, **8**, 40996–41002.

22 S. Priyanka, S. Balasubramanian, *et al.*, First-principles calculations to investigate new ferromagnetic quaternary Heusler alloys FeZrTiZ (Z=Si, Sn, Pb): compatible for spin polarized device and waste heat recovery applications, *Solid State Sci.*, 2022, **132**, 106964.

23 X. T. Wang, H. Khachai, R. Khenata, *et al.*, Structural, electronic, magnetic, half-metallic, mechanical, and thermodynamic properties of the quaternary Heusler compound FeCrRuSi: a first-principles study, *Sci. Rep.*, 2017, **7**, 16183.

24 D. S. Priyanka, J. B. Sudharsan, *et al.*, Cobalt based new quaternary Heusler alloys for spintronic and thermoelectric applications: an ab initio study, *Mater. Technol.*, 2022, **37**, 1–11.

25 P. D. Patel, J. B. Pandya, S. M. Shinde, S. D. Gupta, S. Narayan and P. K. Jha, Investigation of full-Heusler compound Mn_2MgGe for magnetism, spintronics and thermoelectric applications: DFT study, *Comput. Condens. Matter*, 2020, **23**, e00472.

26 R. Prakash, G. Suganya and G. Kalpana, Investigation of novel quaternary Heusler alloys XRuCrZ (X = Co, Ni, Rh, and Pd; Z = Si and Ge) via first-principles calculation for spintronics and thermoelectric applications, *AIP Adv.*, 2022, **12**, 055223.

27 Y. Dhakshayani, G. Suganya and G. Kalpana, DFT studies on electronic, magnetic and thermoelectric properties of half Heusler alloys XCaB (X= Li, Na, K and Rb), *J. Cryst. Growth*, 2022, **583**, 126550.

28 H. Alqurashi, R. Haleoot and B. Hamad, First-principles investigations of Zr-based quaternary Heusler alloys for spintronic and thermoelectric applications, *Comput. Mater. Sci.*, 2022, **210**, 111477.

29 J. Nag, D. Rani, D. Singh, *et al.*, CoFeVSb: a promising candidate for spin valve and thermoelectric applications, *Phys. Rev. B*, 2022, **105**, 144409.

30 S. Idrissi, S. Ziti and H. Labrim, Half-metallic behavior and magnetic proprieties of the quaternary Heusler alloys YFeCrZ (Z=Al, Sb and Sn), *J. Alloys Compd.*, 2020, **820**, 153373.

31 A. Q. Seh and D. C. Gupta, Quaternary Heusler Alloys a Future Perspective for Revolutionizing Conventional Semiconductor Technology, *J. Alloys Compd.*, 2021, **871**, 159560.

32 B. Shi, J. Li, C. Zhang, *et al.*, First-principles investigation on the transport properties of quaternary CoFeRGa (R = Ti, V, Cr, Mn, Cu, and Nb) Heusler compounds, *Phys. Chem. Chem. Phys.*, 2020, **22**, 23185–23194.

33 D. Rabin, D. Fuks and Y. Gelbstein, Alloying effect on the lattice thermal conductivity of MNiSn half-Heusler alloys, *Phys. Chem. Chem. Phys.*, 2023, **25**, 520–528.

34 A. Anjami, A. Boochani, *et al.*, Ab initio study of mechanical, half-metallic and optical properties of Mn_2ZrX (X = Ge, Si) compounds, *Results Phys.*, 2017, **7**, 3522–3529.

35 A. Kalugina, A. Taranova, *et al.*, Thermoelectric properties of Fe1.5TiSb1−xSnx and Fe1.5Ti1−xYxSb Heusler alloys, *Mater. Today: Proc.*, 2021, **44**, 3463–3466.

36 D. Rani, L. Bainsla, K. G. Suresha and A. Alam, Experimental and theoretical investigation on the possible half-metallic behaviour of equiatomic quaternary Heusler alloys: CoRuMnGe and CoRuVZ (Z=Al, Ga), *J. Magn. Magn. Mater.*, 2019, **492**, 165662.

37 K. W. Bae, J. Y. Hwang, S.-I. Kim, *et al.*, Thermoelectric Transport Properties of *n*-Type Sb-doped (Hf, Zr, Ti) NiSn Half-Heusler Alloys Prepared by Temperature-Regulated Melt Spinning and Spark Plasma Sintering, *Appl. Sci.*, 2020, **10**, 4963.

38 Y. Venkateswara, S. S. Samatham, *et al.*, High-TC ferromagnetic inverse Heusler alloys: a comparative study of Fe2RhSi and Fe2RhGe, *Phys. Rev. B*, 2021, **104**, 094402.

39 A. El-Khouly, A. M. Adam, E. M. M. Ibrahim, *et al.*, Mechanical and thermoelectric properties of FeVSb-based half-Heusler alloys, *J. Alloys Compd.*, 2021, **886**, 161308.

40 H. Miyazaki, S.-i. Kimura, K. Onishi, *et al.*, Relation between Electronic Structure and Thermoelectric Properties of Heusler-Type Ru_2VAl Compounds, *Crystals*, 2022, **12**, 1403.

41 C. O. Diasa, J. R. d. M. Monteiroa, *et al.*, Combined Experimental and First Principles Study on Nanostructured NbFeSb Half Heusler Alloy Synthesized by Mechanical Alloying, *Mater. Res.*, 2023, **26**, e20220295.

42 J. P. Perdew, K. Burke and M. Ernzerhof, Generalized gradient approximation made simple, *Phys. Rev. Lett.*, 1996, **77**, 3865–3868.

43 J. P. Perdew, K. Burke and Y. Wang, Generalized gradient approximation for the exchange-correlation hole of a many-electron system, *Phys. Rev. B: Condens. Matter Mater. Phys.*, 1996, **54**, 16533–16539.

44 F. Tran and P. Blaha, Accurate Band Gaps of Semiconductors and Insulators with a Semilocal Exchange-Correlation Potential, *Phys. Rev. Lett.*, 2009, **102**, 226401.

45 J. Drews, U. Eberz and H.-U. Schuster, Optische Untersuchungen an farbigen Intermetallischen phasen, *J. Less-Common Met.*, 1986, **116**, 271–278.

46 D. Murnaghan, The Compressibility of Media under Extreme Pressures, *Proc. Natl. Acad. Sci. U. S. A.*, 1944, **30**, 244–247.

47 F. Birch, Finite Elastic Strain of Cubic Crystals, *Phys. Rev.*, 1947, **71**, 809–824.

48 I. N. Frantsevich, F. F. Voronov and S. A. Bakuta, *Elastic Constants and Elastic Moduli of Metals and Nonmetals*, Naukova Dumka, Kiev, 1982.

49 S. F. Pugh, Relations between the Elastic Moduli and the Plastic Properties of Polycrystalline Pure Metals, *Philos. Mag.*, 1954, **45**, 823–843.

50 D. C. Wallace, *Thermodynamics of crystals*, Wiley, New York, 1972.